JOURNAL OF AIRCRAFT
Vol. 43, No. 3, May–June 2006

Flutter of High-Speed Civil Transport Flexible Semispan Model: Time-Frequency Analysis

Christopher C. Chabalko* and Muhammad R. Hajj†
Virginia Polytechnic Institute and State University, Blacksburg, Virginia 24061-0219
and
Walter A. Silva‡
NASA Langley Research Center, Hampton, Virginia 23681-2199

Time/frequency analysis of fluctuations measured by pressure taps and strain gauges in the experimental studies of the flexible semispan model of a high-speed civil transport wing configuration is performed. The interest is in determining the coupling between the aerodynamic loads and structural motions that led to the hard flutter conditions and loss of the model. The results show that, away from the hard flutter point, the aerodynamic loads at all pressure taps near the wing tip and the structural motions contained the same frequency components. On the other hand, in the flow conditions leading to the hard flutter, the frequency content of the pressure fluctuations near the leading and trailing edges varied significantly. This led to contribution to the structural motions over two frequency ranges. The ratio of these ranges was near 2:1, which suggests the possibility of nonlinear structural coupling.

Introduction

AMONG the complex nonlinear aspects of aeroelastic phenomena are the unsteady nonlinear aerodynamic loads, structural nonlinearities, and fluid–structure interactions.[1] Nonlinearities in aerodynamic loads could originate in the development of shocks and/or flow separation induced by the shock. Structural nonlinearities could be geometric or a result of free play. The fluid–structure interaction could result from nonlinear resonance between the aerodynamic load and structural modes. Under different conditions, one or a combination of these aspects could yield flutter or limit cycle oscillations (LCOs). The overall goal of this work is to develop the capabilities to quantify the role that each of these different nonlinear mechanisms could play in observed flutter and LCOs. The realization of such a goal would help in providing a benchmark for the detection of nonlinear aeroelastic instabilities and possibly effective means for obtaining improved performance and reduced uncertainties through operation beyond conventional boundaries that are based on linear analysis. Additionally, it will help in providing a benchmark for validation of different computational methodologies.

In a set of comprehensive wind-tunnel experiments on a flexible semispan model (FSM) of a high-speed civil transport (HSCT) wing configuration conducted by Silva et al.,[2] two different regions of high dynamic response were observed. Of particular interest to this work is the high dynamic response region that occurred over a large range of dynamic pressures around a Mach number of 0.98. At the top of this region is a "hard" flutter point that resulted in the loss of the model. Hajj and Silva[3] showed that, before this hard flutter point was encountered, a strong shock developed near the trailing edge. Furthermore, and through higher-order spectral analysis of the pressure fluctuations, they showed that, when the shock developed, the aerodynamic forces contained nonlinearly coupled frequency components. The objective of this effort is to extend that work by quantifying the role played by these components in the structural response of the model. This objective is achieved through analysis of the relation between pressure fluctuations at different locations over the wing and of the structural responses as determined from the strain gauges.

Experimental Setup

The experiments were conducted in the Langley Transonic Dynamics Tunnel (TDT) at NASA Langley Research Center. The TDT is specially configured for flutter testing, with excellent model visibility from the control room and a rapid tunnel shutdown capability for model safety (bypass valves). The model planform[2] was a one-twelfth-scale configuration based on an early design known as the reference H configuration. To accommodate pressure instrumentation at the wing tip of the model, the original reference H airfoil thickness was increased to a constant 4% thickness over the entire wing span. Figure 1 shows the planform layout and main components of the model. The leading and trailing edges were removable to access pressure instrumentation in those regions. A removable tip cap allowed access to pressure instrumentation at the wing tip. It should be noted that the FSM was not intended to be a flutter clearance model but, rather, a model that would exhibit an HSCT-like flutter mechanism within the range of operation of the TDT. To induce flutter at around 200 psf (9.57 kPa), a 2.2-lb (1-kg) mass was added to the aft tip section. This mass was fabricated out of tungsten and bonded into the outboard removable trailing-edge section of the FSM (see Fig. 1). Additional reinforcements and local strengthening of the attachment surface between the main wing box and the outboard removable trailing-edge section was performed to handle the added stress of the additional mass.

The instrumentation layout consisted of 131 in situ unsteady pressure transducers located at the 10, 30, 60, and 95% span stations (Fig. 1). Six additional unsteady pressure transducers were installed at the 20% chord station for the 20, 45, and 75% span stations for both upper and lower surfaces. Channels were carved into the foam core to accommodate the wiring for the instrumentation. Specially designed pressure transducer holders were used to eliminate any leakage around the transducer and to provide easy access to the transducers. Instrumentation also included 14 accelerometers installed throughout the wing (Fig. 1). The FSM was instrumented with three bending strain gauges and one torsion strain gauge. All

---

Presented as Paper 2004-1856 at the AIAA/ASME/ASCE/AHS/ASC 45th Structures, Structural Dynamics, and Materials Conference, Palm Springs, CA, 19–22 April 2004; received 1 October 2004; revision received 1 February 2005; accepted for publication 14 February 2005.

*Graduate Research Assistant, 0219 Norris Hall, Department of Engineering Science and Mechanics.

†Professor, 0219 Norris Hall, Department of Engineering Science and Mechanics; mhajj@vt.edu.

‡Senior Research Scientist and Senior Aerospace Engineer, Aeroelasticity Branch, Structures and Materials Competency. Associate Fellow AIAA.

Table 1 Run numbers and test conditions

Run	Mach number	Dynamic pressure, psf
1062	0.922	226.58
1065	0.950	236.00
1066	0.962	240.11
1067	0.967	239.66
Model lost	0.979	245.80

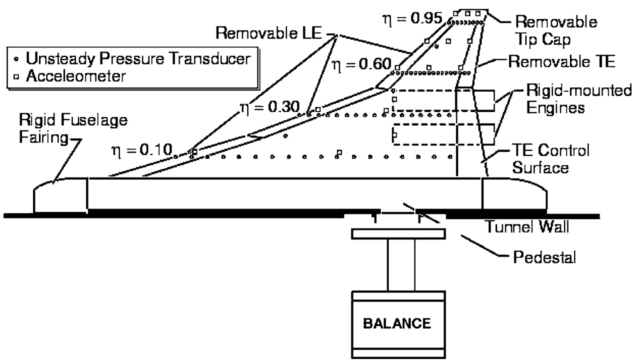

Fig. 1 Planform and instrumentation layout for the FSM wind-tunnel model.

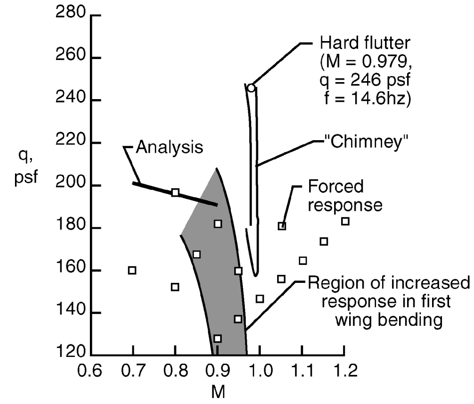

Fig. 2 Summary of the flutter and high-dynamic-response regions for the FSM wind-tunnel model.[2]

gauges were located at midspan, a region of high stresses. One bending strain gauge was placed near the leading edge and will be referred to as the forward strain gauge or FWD. Another was placed near the trailing edge and will be referred to as the aft strain gauge or AFT. The third was placed at midchord and will be referred to as the middle strain gauge or MID. The torsion strain gauge was placed at midchord.

Aerodynamic/Structure Relation

A plot summarizing the dynamic responses that were encountered during flutter testing of the FSM is shown in Fig. 2. Silva et al.[2] provide a detailed discussion of the different regions in this plot. Of particular interest in this figure is the narrow "chimney" region of high dynamic response that spans over a Mach number range from about 0.98 to 1.0 and a deep dynamic pressure range that starts at about 160 psf. At a dynamic pressure of about 250 psf, hard flutter took place, which resulted in the loss of the model. The run number, Mach number, and dynamic pressure of the flow conditions considered here are given in Table 1.

Interpreting the relation between surface pressure fluctuations at a point and the structural response is not straightforward. One issue is the fact that the motion is determined by the integral effect of the pressure fluctuations over the whole surface and not at a point. On the other hand, the flow is completely unsteady and there could be instants when the dynamic relation between an event in the pressure fluctuations at a point and the structural motions is significant. For instance, Fig. 3 shows a part of the simultaneously measured records in run 1065 of the pressure fluctuations at the 80 and 90% chord locations on the upper surface at the 95% span station and of the strain as measured by the aft strain gauge. The pressure measurements at the 90% chord location show that a shock formed ahead of this point. On the other hand, the measurements at the 80% chord location show significant variations in time. The record exhibits nearly periodic variations between times 17.5 and 18.1 s, relatively more random variations with smaller amplitudes between 18.5 and 19.5 s, and a unique intense event near 20 s.

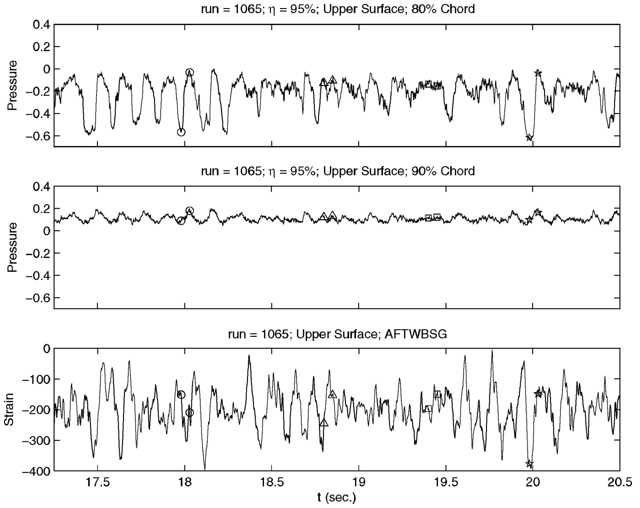

Fig. 3 Part of the simultaneously measured fluctuations from the pressure taps near the trailing edge and the aft strain gauge in run 1065.

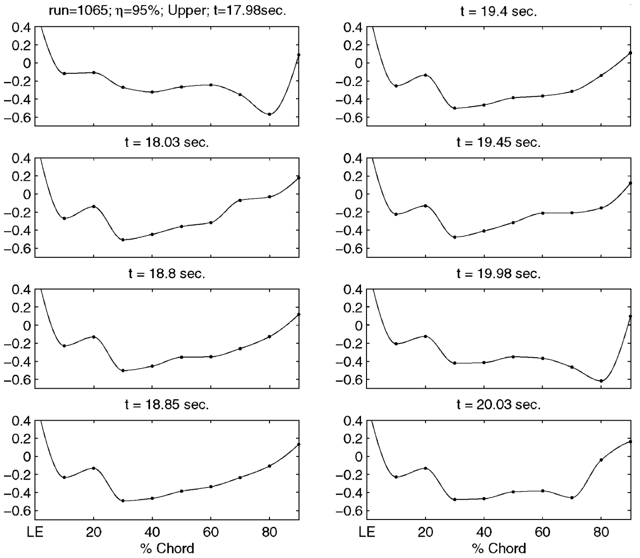

Fig. 4 Pressure variations along the chord at the 95% span location for specific times shown in Fig. 3.

The physical reason for the aforementioned variations can be realized from Fig. 4, which shows the pressure variations along the chord at the 95% span station at specific times in record 1065. The times of the first two plots, 17.98 and 18.03 s, are marked by the open circles in Fig. 3. Obviously, the difference in the measured pressure is associated with the moving shock. The plots in Fig. 4 at times 18.8 and 18.85 s and at 19.4 and 19.45 s do not show a moving shock as observed in the first two plots. These times are marked by the open triangles and squares in Fig. 3. The intense event observed in the pressure fluctuations near $t = 20$ s in Fig. 3 is associated with a shock motion, as observed by the plots at times 19.98 and 20.03 s in Fig. 4. It should also be noted that Fig. 4 shows that the first four taps near the leading edge, up to 40% of the wing, do not exhibit the time variations observed near the trailing edge.

A comparison of the pressure record at the 80% chord location with the measurements by the aft strain gauge in Fig. 3 shows that it is hard to make a direct time correlation between the two records. A Fourier domain analysis of the pressure fluctuations and structural motions will require averaging over time and would yield a vague picture of any significant instantaneous dynamic relations considering the aforementioned variations. On the other hand, an analysis based on the wavelet transform[4] maps the temporal signal onto a time-scale, or time-frequency, domain and would retain any instantaneous relation between the pressure at a point and the structural motions. It should be noted here that both continuous and discrete wavelets have been used in the analysis of aeroelastic signals for different objectives. Lind et al.[5] performed wavelet analysis on a coupled pitch–plunge model that simulates nonlinear flutter observed in experiments conducted at Texas A&M University. The results showed that wavelet maps of free-decay response data can be used to characterize the type of nonlinearity that affects the stiffness. In other studies, wavelet analysis has been performed to filter flight data, which allowed for reduction in the uncertainity of aeroservoelastic stability margins[6] or faster identification of flutter boundaries.[7] This work presents yet another use of wavelet analysis in that it is used for the detection of the coupling between the aerodynamic loading and the structural response in an aeroelastic system. In the nest section, a summary is given of the wavelet analysis procedure and specifics followed in this work. Variations in the time-frequency characteristics of strain and pressure measurements over the range of flow conditions presented in Table 1 and that include one condition away from this flutter point and three conditions leading to the point where the hard flutter is encountered are presented in the next section.

Data Analysis

The continuous wavelet transform, $W(a,\tau)$, of a function $g(t)$ is defined as the inner product between $g(t)$ and the wavelet family $\Psi(a,t)$:

$$W(a,\tau) = \int_{-\infty}^{\infty} g(t)\Psi^*(a, t-\tau)\,\mathrm{d}t \tag{1}$$

The wavelet coefficients $W(a,\tau)$ represent the contribution to $g(t)$ of scale a at a time τ. The wavelet family $\Psi(a,t)$ is generated from a mother wavelet $\Psi(t)$ by continuous translations of τ and dilations of a. Any real- or complex-valued function can be considered a mother wavelet as long as it satisfies the admissibility condition:

$$\int_{-\infty}^{\infty} \frac{|\hat{\Psi}(\omega)|^2}{\omega} < \infty \tag{2}$$

where $\hat{\Psi}(\omega)$ is the Fourier transform of $\Psi(t)$. The admissibility condition means that the wavelet has a zero offset and finite bandwidth and gain. In the time domain, this condition is expressed as the requirement that the wavelet has a zero mean and finite temporal support.

One common complex wavelet is the Morlet wavelet, where the mother wavelet is given by a sinusoid multiplied by a Gaussian function:

$$\Psi(t) = e^{i\omega_\psi t}e^{-t^2/2} \tag{3}$$

where ω_ψ is the nondimensional peak frequency of the wavelet and has a value of 5.5. This value yields a mean for the Morlet wavelet of -0.000106 to approximately satisfy the admissibility condition. Because the wavelet function has a Gaussian distribution in the frequency domain, there is not a one-to-one correspondence between frequency and scale. However, because of the bandpass filter nature of Fourier-transformed wavelets, one can determine a relationship between the scale, a, and the peak frequency, f_p, of the bandpass filter corresponding to each scaled wavelet. This relationship was derived by Jordan et al.[8] and in this work it was determined to be

$$f_p = 437.5/a \tag{4}$$

with f_p in hertz. From the wavelet transform coefficients, $W(a,\tau)$, the wavelet energy in the time-scale domain is defined as WW^*, which is also known as the scalogram. The wavelet energy gives a measure of the energy contained by the different scales as a function of time. For the purpose of determining the relation between the surface pressure fluctuations at a point and the structural motions, the cross scalogram is used. The cross scalogram between two functions, $f(t)$ and $g(t)$, is defined as $W(f)W^*(g)$. It gives an indication of the occurrence of fluctuations of the same scale at the same time in two simultaneous time series.

Results and Discussion

Contour plots of the wavelet energy of the fluctuations measured by the three bending strain gauges at the test conditions presented in Table 1 are shown in Figs. 5–8. In run 1062 (Fig. 5), the forward and midstrain gauges show high-level energy peaks that are accompanied by streaks that extend over a range of frequencies between 12.5 and 17 Hz. These peaks take place at the same time in both gauges. At the aft strain gauge, the energy is more concentrated near a frequency of 12.5 Hz.

In contrast with the one high-energy frequency range that characterizes the strain-gauge fluctuations in run 1062, the distribution of energy in runs 1065 and 1066, presented in Figs. 6 and 7, shows two separated ranges of frequency components with high energy peaks.

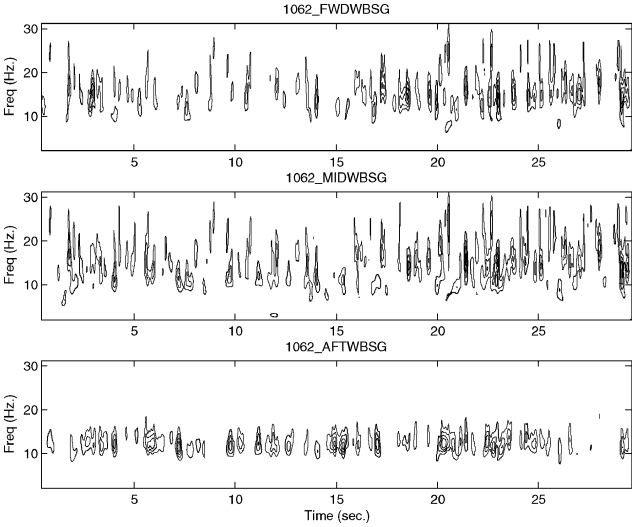

Fig. 5 Wavelet energy of the fluctuations measured by the forward, mid-, and aft strain gauges for run 1062.

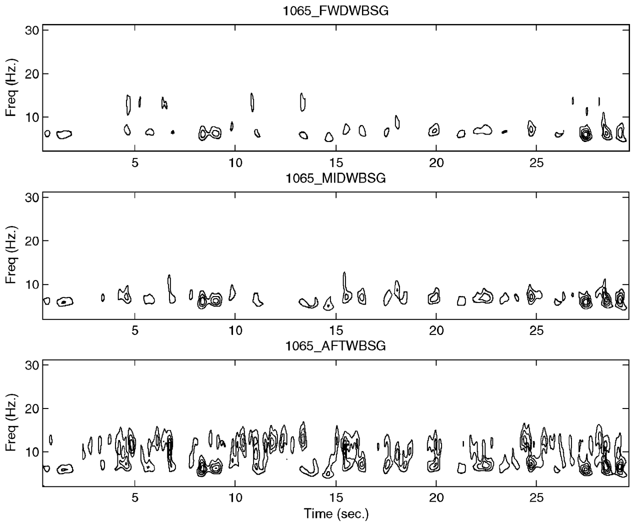

Fig. 6 Wavelet energy of the fluctuations measured by the forward, mid-, and aft strain gauges for run 1065.

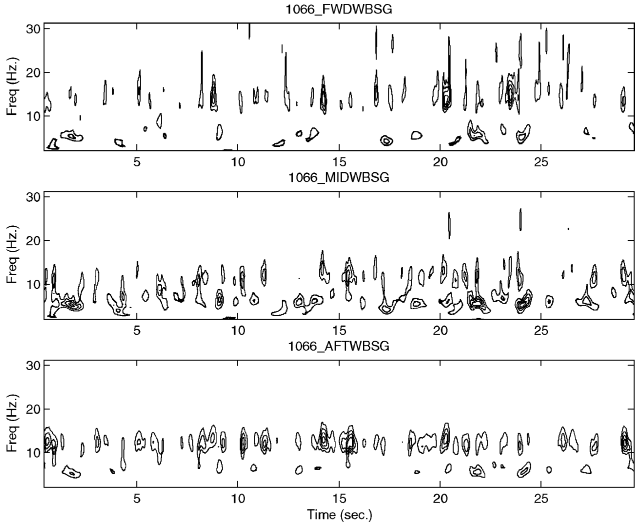

Fig. 7 Wavelet energy of the fluctuations measured by the forward, mid-, and aft strain gauges for run 1066.

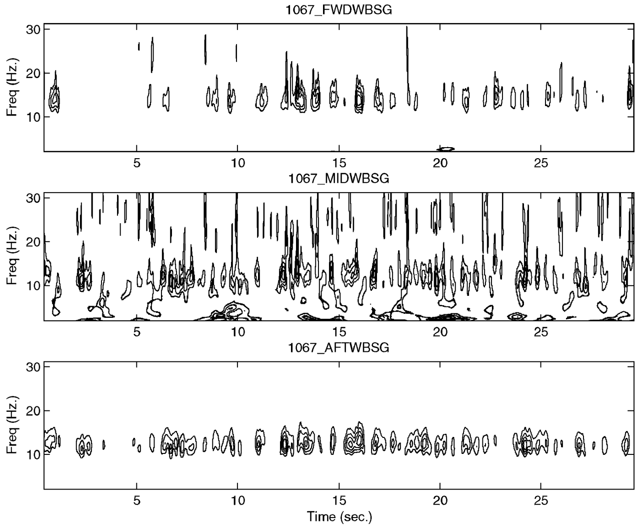

Fig. 8 Wavelet energy of the fluctuations measured by the forward, mid-, and aft strain gauges for run 1067.

In run 1065, and in all strain gauges, most of the energy is contained at the low-frequency components between 5.7 and 6.8 Hz. A second component that contains energy is near 12.5 Hz and extends at different times over a range between 11.5 and 13.5 Hz. Although the level of energy over this latter range is at the same level as that at the lower frequencies in the aft strain gauge, it is much smaller in the mid- and forward strain gauges. The presence of two separate ranges with high-energy peaks is also noted in run 1066. At the forward and midstrain gauges, peaks are noted in the frequency range between 12.5 and 14.3 Hz and near 5.4 Hz. At the aft strain gauge, the energy is distributed in two ranges, between 11.3 and 13 Hz and between 5.4 and 6.6 Hz. A closer look at the two separated frequency ranges in both runs 1065 and 1066 in the aft strain gauge shows that, within the resolution of the wavelet analysis as performed here, the two ranges of peaks have a 2:1 ratio. This ratio implies the possibility of nonlinear coupling of the frequency components in the structural response.

In run 1067, the time-frequency analysis of the measured strain at the three strain gauges also shows two separated frequency ranges with high energy. At the forward and midstrain gauges, the highest peak extends over the range between 12.5 and 14.3 Hz, with a smaller peak at the lowest measured frequency of 0.5 Hz. At the aft strain gauge, the highest peak is near 12.5 Hz. Again, a smaller peak is noted to appear intermittently, at the lowest measured frequency of 0.5 Hz. Through comparisons of the magnitude of the wavelet coefficients for all measurements just presented, it is noted that the energy peaks in the aft strain gauge are always concentrated over a smaller range of frequencies than the peaks in the mid- and forward strain gauges.

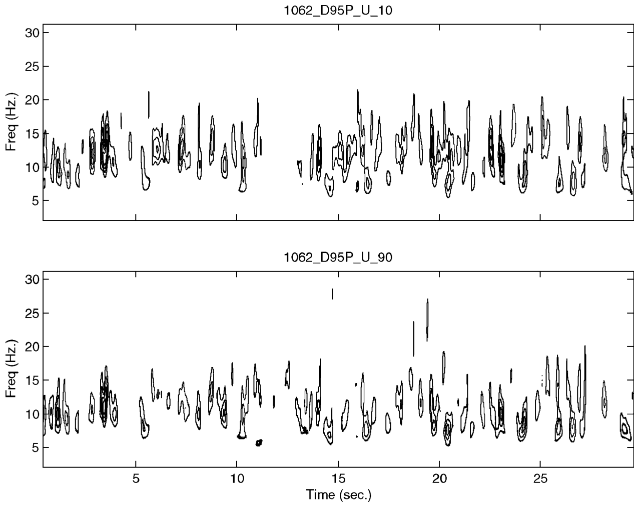

Fig. 9 Wavelet energy of the pressure fluctuations measured at $x/c = 10\%$ and 90% of the chord at 95% of the span in run 1062.

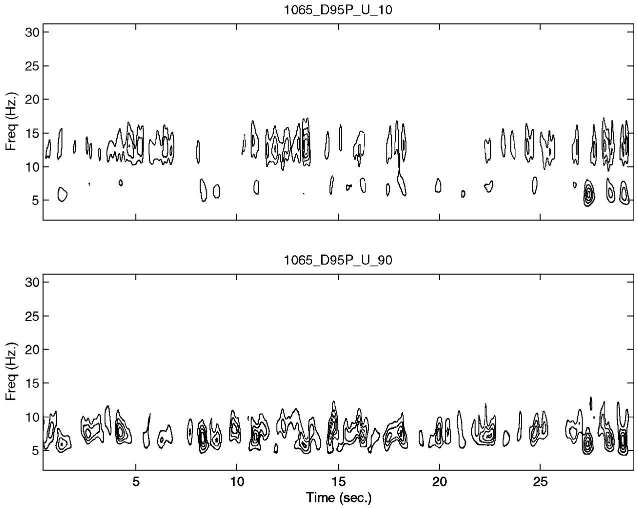

Fig. 10 Wavelet energy of the pressure fluctuations measured at $x/c = 10\%$ and 90% of the chord at 95% of the span in run 1065.

Wavelet analysis was also performed on the pressure fluctuations measured at the 95% span location. Figures 9–12 show the magnitude of the wavelet coefficients of the pressure fluctuations measured on the upper surface near the leading and trailing edges in runs 1062, 1065, 1066, and 1067, respectively. In run 1062, the results show that high-energy events in the pressure fluctuations at both 10 and 90% chord locations take place simultaneously and at the same frequency component. This characteristic is completely reversed in runs 1065, 1066, and 1067. In all of these runs, most of the energy at the 10% chord location is in the frequency components that are between 11 and 14.5 Hz. On the other hand, at the 90% chord location, the energy is mostly in a lower frequency range, between 5 and 7 Hz, in runs 1065 and 1066 and between 5 and 0.5 Hz in run 1067. These results show that, as the flutter point was encountered, the leading and trailing edges near the wing tip were experiencing different aerodynamic loads. Detailed analysis of other pressure taps showed that the contribution to the high-frequency components in runs 1065, 1066, and 1067 is from aerodynamic pressure fluctuations that extend all the way up to the 30% chord location. The rest of the wing is subjected to the lower frequencies of pressure fluctuations. Of equal interest is the synchronization between the

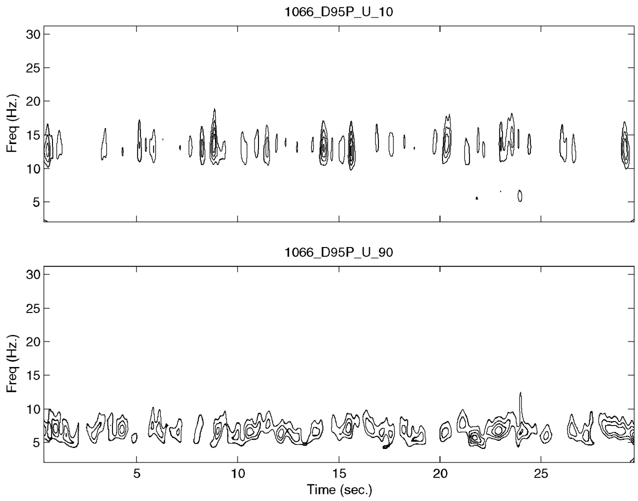

Fig. 11 Wavelet energy of the pressure fluctuations measured at $x/c = 10\%$ and 90% of the chord at 95% of the span in run 1066.

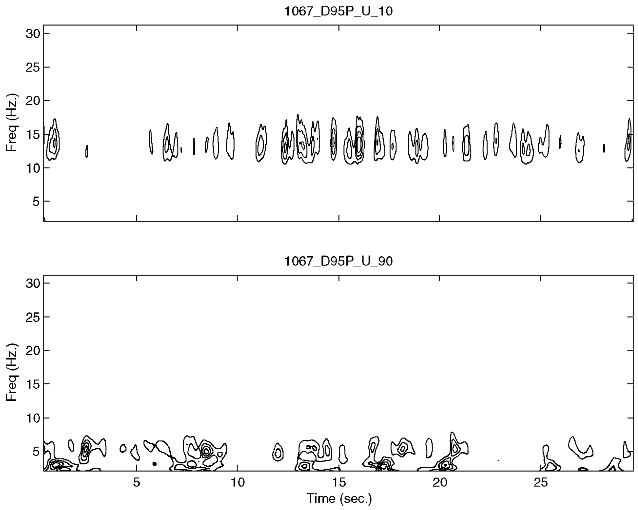

Fig. 12 Wavelet energy of the pressure fluctuations measured at $x/c = 10\%$ and 90% of the chord at 95% of the span in run 1067.

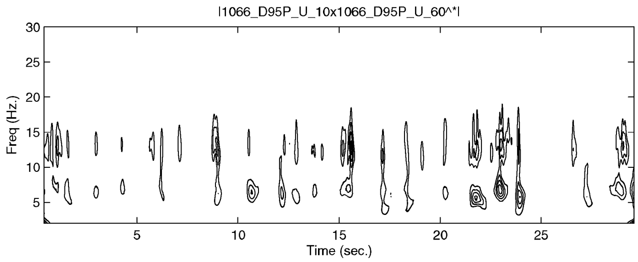

Fig. 13 Magnitude of the wavelet cross scalogram between the pressure fluctuations measured at $x/c = 10\%$ and 60% of the chord at 95% of the span in run 1066.

higher- and lower-frequency components of the aerodynamic load on the different parts of the wing near the tip. Figure 13 shows the wavelet cross scalogram between the pressure fluctuations measured at the 10 and 60% chord locations in run 1066. The magnitude of the cross scalogram is large when fluctuations from two time series coincide in scale and time. If fluctuations do not appear at the same time and same scale, the magnitude of the cross scalogram is very low. The results clearly show that the amplitude variations of the high- and low-frequency components of the aerodynamic load are synchronized in time. This implies their phase coupling and interactions.

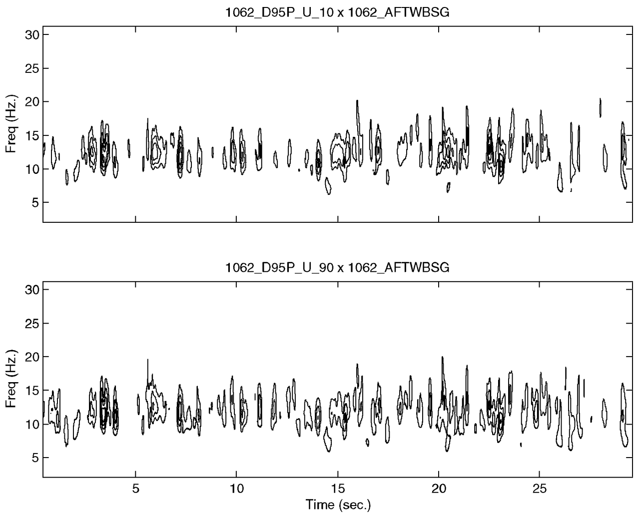

Fig. 14 Magnitude of the wavelet cross scalogram between the fluctuations measured at the aft strain gauge and the pressure taps for run 1062.

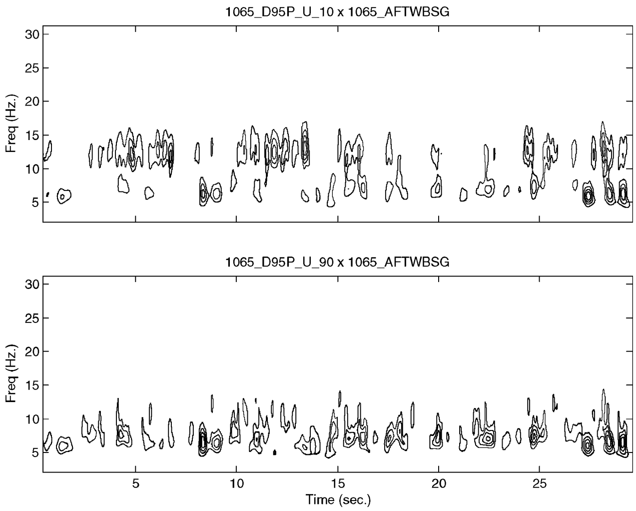

Fig. 15 Magnitude of the wavelet cross scalogram between the fluctuations measured at the aft strain gauge and the pressure taps for run 1065.

Using the cross scalogram between the motions measured by strain gauges and the surface pressure fluctuations from different taps, one can examine the role of different frequency components as measured at these taps in contributing to the structural motions. Figures 14–17 show the magnitude of the cross scalogram between fluctuations of the surface pressure measured near the leading and trailing edges and of the aft strain gauge in runs 1062, 1065, 1066, and 1067, respectively. In run 1062, it is obvious that the contribution to the motions from both the 10 and 90% taps takes place over the same frequency range and at the same time. In contrast, Figs. 15–17 show that the contribution to the relatively high range of frequency fluctuations, between 11 and 14.5 Hz, is mostly from the aerodynamic load at the leading edge. The contribution at the lower-frequency range, between 5 and 7 Hz in runs 1065 and 1066 and near 0.5 Hz in run 1067, is mostly from the aerodynamic load near the trailing edge.

The aforementioned results provide new insights into the different aspects of the flutter of the FSM model. First, away from the flutter region, the aerodynamic load near the wing tip was uniform over the whole chord. Additionally, the frequency components with the highest energy in both fluctuations of the surface pressures and aft strain gauge are the same. Second, as flutter conditions were approached, the frequency content of the aerodynamic loads over the wing tip varied significantly. Near the leading edge, the pressure fluctuations

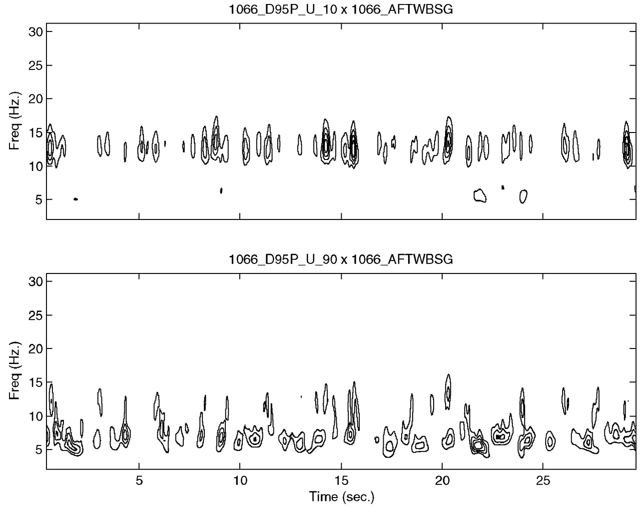

Fig. 16 Magnitude of the wavelet cross scalogram between the fluctuations measured at the aft strain gauge and the pressure taps for run 1066.

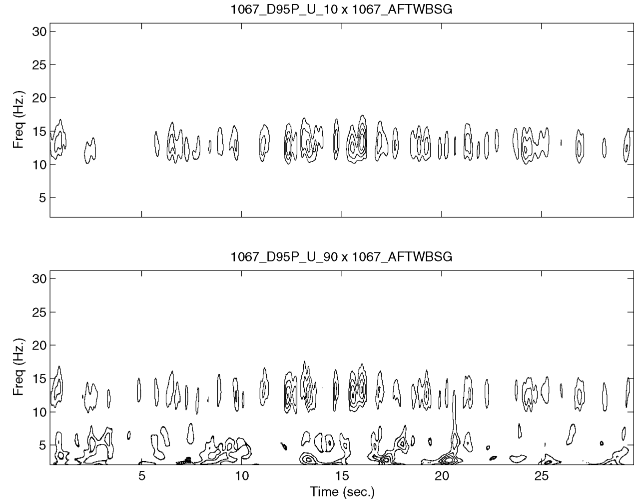

Fig. 17 Magnitude of the wavelet cross scalogram between the fluctuations measured at the aft strain gauge and the pressure taps for run 1067.

contained relatively large frequency components that are close to those measured away from the flutter region. On the other hand, the aerodynamic loads near the trailing edge were characterized by a lower range of frequency components. Cross-scalogram analysis of the relation between the pressure fluctuations near the leading and trailing edges and the aft strain gauges showed a significant contribution of both frequency ranges to the structural motions. Third, it is of interest to note that the ratio of these frequency ranges was about 2:1.

In comparison to the aspects just discussed, the linear aeroelastic analyses presented by Schuster et al.[9] and Baker et al.[10] show that the mechanisms leading to the flutter of the FSM model involve the coalescence of two modes. In particular, the critical mechanism that caused the flutter involved a continuous increase in the frequency (stiffening) of the first mode with the increase in the dynamic pressure to match that of the third mode. This matching caused an enhanced response of the third mode. Noting that the first four modes, based on ground vibration tests, have frequencies of 8.06, 9.7, 15.27, and 18.87 Hz,[2,9] one would conclude that the linear analyses did not predict any role played by the aerodynamic loads and structural response at the lower range of frequencies. On the other hand, the analysis presented here shows that aerodynamic loads over the lower-frequency range as detected near the trailing edge, and over the higher-frequency range as detected near the leading edge, enhanced the higher-frequency range in the structural response, which happens to be near one of the structural modes, namely, mode 3 of the wing model. Finally, it should be noted that the damping and structural nonlinearities in the FSM model could have been identified by performing experiments whereby nonlinearities were exploited. Hajj et al.[11] presented a procedure that combines amplitudes and phases of higher-order spectral moments estimated from data measured under nonlinear excitation conditions with approximate solutions of governing equations or parameters to characterize damping and identify the type of nonlinearities. Unfortunately, such experiments were not performed for the FSM model.

Conclusions

In this work, wavelet analysis is performed to determine the time-frequency variations of fluctuations measured by pressure taps and strain gauges in the experimental studies of the FSM of an HSCT wing configuration. The wavelet energy is used to determine the energy content of theses fluctuations and the cross scalogram is used to determine the relation between aerodynamic load near the wing tip as measured by the pressure taps and the structural motions as exhibited by the aft strain gauge. The interest is in the hard flutter conditions that lead to the loss of the model. The results show that, away from the hard flutter point, the aerodynamic loads at all pressure taps near the wing tip and the structural motions contained the same frequency components. On the other hand, in the flow conditions leading to the hard flutter, the frequency content of the pressure fluctuations near the leading and trailing edges varied significantly. This led to a contribution over two frequency ranges to the structural motions as measured by the aft strain gauge. The ratio of these ranges was near 2:1, which suggests the possibility of nonlinear structural coupling.

Acknowledgments

The support of the Air Force Office of Scientific Research through grant F49620-03-1-0206 and of the National Institute of Aerospace through grant VT-03-01, subnumber 3044-VT, supplement 7, is acknowledged.

References

[1] Dowell, E., Edwards, J., and Stragnac, T., "Nonlinear Areoelasticity," *Journal of Aircraft*, Vol. 40, No. 5, 2003, pp. 857–874.

[2] Silva, W. A., Keller, D. F., Florance, J. R., Cole, S. R., and Scott, R. C., "Experimental Steady and Unsteady Aerodynamic and Flutter Results for HSCT Semispan Models," AIAA Paper 2000-1697, April 2000.

[3] Hajj, M. R., and Silva, W. A., "Nonlinear Flutter Aspects of the Flexible HSCT Semispan Model," *Journal of Aircraft*, Vol. 41, No. 5, 2004, pp. 1202–1208.

[4] Addison, P. S., *The Illustrated Wavelet Transform Handbook: Introductory Theory and Applications in Science, Engineering, Medicine and Finance*, Institute of Physics, Bristol, Philadelphia, 2002.

[5] Lind, R., Snyder, K., and Brenner, M., "Wavelet Analysis to Characterize Non-Linearities and Predict Limit Cycles of an Aeroelastic System," *Mechanical Systems and Signal Processing*, Vol. 15, No. 2, 2001, pp. 337–356.

[6] Brenner, M., and Lind, R., "Wavelet-Processed Flight Data for Robust Aeroservoelastic Stability Margins," *Journal of Guidance, Control, and Dynamics*, Vol. 21, No. 6, 1998, pp. 823–829.

[7] Johnson, J. D., Lu, J., Dhawan, A. P., and Lind, R., "Real-Time Identification of Flutter Boundaries Using the Discrete Wavelet Transform," *Journal of Guidance, Control, and Dynamics*, Vol. 25, No. 2, 2002, pp. 334–339.

[8] Jordan, D. A., Miksad, R. W., and Powers, E. J., "Implementation of the Continuous Wavelet Transform for Digital Time Series Analysis," *Review of Scientific Instrumentation*, Vol. 68, No. 3, 1997, pp. 1484–1494.

[9] Schuster, D. M., Spain, C. V., Turnock, D. L., Rausch, R. D., Hamouda, M.-N., Vogler, W. A., and Stockwell, A. E., "Development, Analysis, and Testing of the High Speed Research Flexible Semispan Model," NASA CR 1999-209556, Sept. 1999.

[10] Baker, M. L., Mendoza, R., and Hartwich, P. M., "Transonic Aeroelastic Analysis of a High Speed Transport Wind Tunnel Model," AIAA Paper 99-1217, April 1999.

[11] Hajj, M. R., Fung, J., Nayfeh, A. H., and Fahey, S. O., "Damping Identification Using Perturbation Techniques and Higher-Order Spectra," *Nonlinear Dynamics*, Vol. 23, No. 3, 2000, pp. 189–203.